Monitoring of Snow Surface Near-Infrared Bidirectional Reflectance Factors with Added Light Absorbing Particles

Adam Schneider[1], Mark Flanner[1], Roger De Roo[1], and Alden Adolph[2]

[1]Department of Climate and Space Sciences and Engineering, Climate & Space Research Building, University of Michigan, 2455 Hayward St., Ann Arbor, MI 48109-2143
[2]Physics Department, St. Olaf College, 1520 St. Olaf Ave., Northfield, MN 55057

Correspondence: Adam Schneider (amschne@umich.edu)

Abstract. Broadband snow albedo can range from 0.3 to 0.9 depending on microphysical properties and light absorbing particle (LAP) concentrations. Beyond the widely observed direct and visibly apparent effect of darkening snow, it is still unclear how LAPs influence snow albedo feedbacks. To investigate LAPs' indirect effect on snow albedo feedbacks, we developed and calibrated the Near-Infrared Emitting and Reflectance-Monitoring Dome (NERD) and monitored bidirectional reflectance
5 factors (BRFs) hourly after depositing dust and black carbon (BC) particles onto experimental snow surfaces. After comparing snow infrared BRFs to snow SSA, we found that both measured and modeled snow infrared BRFs are correlated with snow SSA. These results, however, demonstrate a considerable uncertainty of $+/- 10 \text{ m}^2\text{kg}^{-1}$ in the determination of snow SSA from our BRF measurements. The nondestructive technique for snow SSA retrieval presented here can be further developed for science applications that require rapid in situ snow SSA measurements. After adding large amounts of dust and BC to snow,
10 we found more rapid decreasing of snow BRFs and SSA in snow with added LAPs compared to natural (clean) snow, but only during clear sky conditions. These results suggest that deposition of LAPs onto snow can accelerate snow metamorphism via a net positive snow grain-size feedback.

1 Introduction

Snow cover modulates Earth's surface energy budget by reflecting a large portion of the incident solar radiative energy flux.
15 As snow melts, more absorptive surfaces are uncovered resulting in a positive feedback mechanism known as the snow albedo feedback (SAF) (Qu and Hall, 2007; Hall, 2004). Light absorbing particles (LAPs) within the snowpack, including elemental (black) carbon (BC), brown carbon, dust, and microbes, directly decrease snow albedo which can initiate the SAF and accelerate snow melt (Bond et al., 2013; Qian et al., 2015; Skiles et al., 2018). Hadley and Kirchstetter (2012) experimentally verified that the reduction of snow albedo due to BC is enhanced for larger snow grains, implying a possible positive "grain-size" feedback
20 induced by impurities in the snow. This positive feedback can also be inferred from the spectral snow albedo models presented by Warren and Wiscombe (1980) and from the Snow, Ice, and Aerosol Radiation (SNICAR) model (Flanner et al., 2007, 2009). Generally, two-layer models that represent snowpack as a collection of spheres can reproduce spectral hemispherical reflectances that compare well with observations (Grenfell et al., 1994).

Snow grain size is often quantified by its optically equivalent sphere effective radius, r_e, which is related to specific surface area, SSA, such that SSA = $3/(\rho_{ice} r_e)$, where ρ_{ice} is the density of pure ice (917 kg/m^3 at 0° C). Snow SSA is defined as the total ice-air interfacial surface area S to ice mass m ratio, such that

$$\text{SSA} = S/m = \frac{S}{\rho_{ice} V}, \tag{1}$$

expressed in terms of its total ice mass or volume V (Hagenmuller et al., 2016; Gallet et al., 2014). In snowpack with large temperature gradients, the diffusion of vapor causes snow SSA to decrease during the natural process of snow metamorphism (Flanner and Zender, 2006; Wang and Baker, 2014). In the absence of a temperature gradient, an isothermal snowpack with snow grains with low radii of curvature undergo coarsening in a process driven by the Kelvin effect. Ebner et al. (2015) show that measurements of snow SSA evolution in isothermal snow agree with the isothermal snow metamorphism modeling framework developed by Legagneux et al. (2004) and Legagneux and Domine (2005). These laboratory studies express snow SSA in isothermal metamorphism as a function of time t as follows,

$$\text{SSA}(t) = \text{SSA}_0 \left(\frac{\tau}{\tau + t} \right)^{1/n}, \tag{2}$$

for initial snow SSA$_0$ at $t = 0$, growth rate parameter τ, and growth exponent n.

Snow SSA strongly affects absorption of infrared radiation. This relationship is evident from measurements of infrared reflectance that are highly correlated with snow SSA for various snow types (Domine et al., 2006). Among others, Gallet et al. (2009) and Gallet et al. (2014) exploit this correlation in the determination of dry snow SSA and wet snow SSA, respectively, using 1.31 µm directional hemispherical reflectance measurements (1.55 µm for measurements of snow SSA > 60 m^{2}kg^{-1}). Arnaud et al. (2011) present the Profiler Of snow SSA Using SWIR reflectance Measurement (POSSUM), which applies the theoretical formulations from Kokhanovsky and Zege (2004) and Picard et al. (2009) to derive snow SSA from hemispherically averaged bidirectional reflectance measurements. Other studies establish techniques to obtain snow SSA using methane gas absorption (Legagneux et al., 2002) and X-ray micro-computed tomography (X-CT) in cold rooms (Pinzer and Schneebeli, 2009). Matzl and Schneebeli (2006) also derive snow SSA using infrared photography. Other techniques that are nondestructive enable the rapid retrieval of snow effective radius r_e from field measurements. Gergely et al. (2014), for example, demonstrate a technique to quickly determine the snow optically equivalent diameter from 0.95 µm bi-hemispherical reflectance measurements. Painter et al. (2007) infer snow r_e from spectral hemispherical directional reflectance factor measurements using a contact probe and a spectrometer.

While previous studies monitor snow metamorphism in clean snow, in situ experimentation of how LAPs affect the snow grain-size feedback diurnally in natural environments is challenging. These challenges can be partly attributed to the limited availability of inexpensive snow SSA measurement devices that can operate quickly in the field, and to the numerous constraints on being able to reproduce naturally occurring conditions for which LAPs in snow strongly influence the climate system. While the POSSUM is a suitable instrument for this study, here, our first objective is to demonstrate the utility of a new instrument we use to quickly obtain approximate snow *surface* SSA (with LAPs). Our second objective is to investigate the effects of added LAPs on the snow grain-size feedback.

In the following sections, we first describe a numerical model that simulates multiple scattering in three dimensions to aid the design and calibration of the Near-Infrared Emitting and Reflectance Monitoring Dome (NERD). Next, we describe the NERD apparatus, which enables multiple 1.30 and 1.55 μm bidirectional reflectance factor (BRF) measurements in just minutes while minimally altering the snow structure. To calibrate the NERD with respect to snow SSA, we then compare snow BRFs with X-CT derived SSA and develop an empirical relationship between measured SSA and snow 1.30 μm BRFs. Finally, we discuss results from our LAP in snow experiments in which we monitored accelerated snow metamorphism. Overall, this study demonstrates the NERD measurement technique and conditions for which the snow grain-size feedback can be enhanced by the presence of LAPs.

2 Instrumentation and Methods

2.1 Monte Carlo Modeling of Multiple Scattering in Snowpack

The Monte Carlo method is applied to numerically simulate three dimensional (3D) light scattering within an idealized snowpack. Gaussian distributions (with 0.085 and 0.130 μm full width at half-maximums) of photon wavelengths (centered around 1.30 and 1.55 μm) were selected to model light emission by narrow-band infrared light emitting diodes (LEDs). One by one, photons are initiated downward into the snow medium, as demonstrated by Kaempfer et al. (2007), and propagated in optical depth space. Extinction, absorption, and polarization are accounted for following the scattering approach for geometrical optics described by Malinka (2014). Accordingly, random numbers (RN_i) in the interval (0, 1) are generated to determine the photon optical path lengths, l_i, such that

$$l_i = \ln(1/RN_i) \tag{3}$$

before the first scattering event ($i = 0$) and again after each scattering event i. Absorption (and termination) of a photon can occur during a scattering event if an additionally generated random number (between 0 and 1) is greater than the particle's single scattering albedo. When a photon is scattered, its new direction cosines are determined from an optimized "rejection method" using the particles' scattering matrices (Ramella-Roman et al., 2005).

To calculate snow BRFs, 1,000,000 photons are propagated and traced through modeled snowpack until they are absorbed or exit the medium. The snowpack is modeled as two phase (air and ice) media containing a regular arrangement of suspended homogenous ice particles. Aspherical particle single scattering properties, including the mass absorption cross sections, asymmetry parameters, single scattering albedos, projected areas, volumes, and scattering matrices were calculated by Yang et al. (2013) for randomly oriented droxtals and solid hexagonal columns. For spheres, Mie Theory is applied, but with the analytical Henyey-Greenstein phase function (van de Hulst, 1968) to improve computational efficiency. The subset of shape habits (smooth droxtals and hexagonal columns) from the large dataset provided by Yang et al. (2013) was selected because these shape habits are purely convex solid ice. Because they are solid convex bodies, their SSAs can be computed from the their projected areas and volumes (Vouk, 1948). Azimuthal mean BRFs are calculated according to the reflectance definitions presented by Dumont et al. (2010) Hudson et al. (2006), and Nicodemus et al. (1977). Accordingly, photon exit angles are grouped into

30 exit zenith angle (θ_r) bins at three degree resolution. Azimuthal (ϕ) mean BRFs are calculated by zenith angle, θ_r, from the total incident photon flux, Φ_i (at a given θ_i), from

$$R(\theta_i; \theta_r) = (2\Phi_i \sin\theta_r \cos\theta_r)^{-1} \int\limits_0^{2\pi} d\Phi_r d\phi, \tag{4}$$

where $d\Phi_r$ represents the reflected photon flux through discrete solid angle bins. In the denominator, the $\cos\theta_r$ factor satisfies
5 Lambert's cosine law while $\sin\theta_r$ accounts for the zenith angular dependence of the azimuthally integrated projected solid angle. Finally, the factor two is necessary to normalize the resulting weighting function $w(\theta_r) = \sin\theta_r \cos\theta_r$, as

$$\int\limits_0^{\pi/2} \sin\theta_r \cos\theta_r d\theta = \frac{1}{2}. \tag{5}$$

Statistical uncertainty was determined by computing BRFs from simulations of Lambertian surfaces and tested using different numbers of photons. Azimuthal averaging reduces the BRFs' dimensionality, so that fewer photons are needed to mitigate
10 Monte Carlo noise. Eq. 4 was initially applied to Monte Carlo simulations of 75 thousand photons reflected by various ideal Lambertian surfaces. At three degree (zenith angular) resolution, 30 and 60 degree BRFs of Lambertian surfaces were simulated accurately to within +/- 2 %. This margin of uncertainty was determined by computing RMS differences between calculated and specified Lambertian reflectances ranging from 0 to 1. Across this range, RMS differences at 30 and 60 degrees were generally less than 0.01. In subsequent test cases, simulating snowpack BRFs with up to 10,000,000 photons did not signifi-
15 cantly change results when compared with simulations of 250,000 photons. Ultimately, it was determined that simulations with 1,000,000 photons were appropriate for the remainder of this study.

2.2 Near-Infrared Bidirectional Reflectance Factor Measurements

The NERD is designed to measure 1.30 and 1.55 µm BRFs. These wavelengths are selected for snow SSA retrieval due to the strong dependence of snow albedo on grain size in these parts of the spectrum. Snow spectral albedo is simulated here using
20 the SNICAR model to demonstrate this sensitivity (Fig. 1). While snow spectral albedo is sensitive to snow effective radius r_e (and thus snow SSA), it is not sensitive to small black carbon concentrations at these wavelengths. Snow SSA can therefore be retrieved using 1.30 µm and 1.55 µm reflectance measurements for snow with small black carbon concentrations.

The design principle is similar to the DUal Frequency Integrating Sphere for Snow SSA measurements (DUFISSS) (Gallet et al., 2009). The NERD also uses 1.30 (1.31 in DUFISSS) and 1.55 µm emitters to illuminate the snow surface from nadir (15
25 degrees off nadir for 1.55 µm in NERD). The main distinction between the DUFISSS and the NERD is the type of reflectance measured. Gallet et al. (2009) use an integrating sphere to measure hemispherical reflectance. In the NERD, however, photodiodes are directed toward the illuminated surface in a black dome to measure BRFs, as demonstrated by Arnaud et al. (2011). The interior of the dome is painted with a flat black paint to increase absorptivity and minimize internal reflections between the dome and snow surface. To test the near-infrared absorptivity of the black pigment, the NERD was used to measure BRFs
30 of a painted black surface. All measured BRFs of the black surface were less than 0.03.

Four infrared light emitting diodes (LEDs) are mounted into the 17 cm diameter black styrene half-sphere. Two LEDs with peak emission wavelengths of 1.30 µm are mounted at nadir and ten degrees relative to zenith and two LEDs with peak emission wavelengths of 1.55 µm are mounted at 15 degrees off nadir (see Fig. 2). The 1.30 µm LEDs have spectral line half widths of 0.085 µm and half intensity beam angles of ten degrees, while the 1.55 µm LEDs have half-maximum bandwidths

5   of 0.130 µm and 20 degree beam angles. These high powered, narrow beam infrared LEDs were selected to illuminate a small oval (estimated major axes of 1.5 cm at 1.30 µm and 3.0 cm at 1.55 µm) of the experimental surface to maximize the reflected radiance signal. The reflected radiance signal is measured using four InGaAs photodiodes mounted in two different azimuthal planes (0 and 90 degrees relative to the illumination); two each at 30 and 60 degrees relative to zenith. Photodiodes highly sensitive to light with wavelengths ranging from 0.80 to 1.75 µm and relatively large active areas (1 mm) were selected to

10 maximize sensitivity.

Because the orientation of LEDs and photodiodes are fixed, reflectance factors of surfaces with negligible subsurface scattering can be obtained after calibration using two diffuse reflectance targets (Gallet et al., 2009; Gergely et al., 2014; Dumont et al., 2010). These Lambertian targets reflect incident light according to Lambert's cosine law and appear equally bright at all viewing angles. By comparing the measured voltage signal from the experimental (snow) surface to that measured from the

15 reflectance targets, two BRFs at both 30 and 60 degree viewing angles are obtained for each light source. While subsurface scattering of visible light in snow is pervasive (Smith et al., 2018), the light penetration in snow near 1.30 and 1.55 µm is at most a couple centimeters due to the strong absorption features in the near-infrared (Kaempfer et al., 2007; Grenfell et al., 1994; Brandt and Warren, 1993). Subsurface scattering is therefore assumed to be minimal and fully contained within each photodiode's field of view.

20 To validate NERD reflectance measurement accuracy, precision, and responsiveness, measured BRFs of reflectance standards are recorded after calibration. BRFs (R) for each LED / photodiode viewing zenith angle ($\theta_i; \theta_r$) combination are measured in temperatures ranging from -20 ° to +2 °C. In general, NERD BRFs of the Lambertian reflectance standards are accurate to within +/- 2 %. We quantify instrument precision (2 %) by computing root mean squared (RMS) differences from repeated measurements (see Table 1). Linear regressions quantify the linear response (A) over the reflectance range of 0.41 to

25 0.95. Response uncertainty ranges from -2 % to +3 % and from +1 % to +3 % at 1.30 and 1.55 µm, respectively. These test results indicate the NERD's ability to obtain BRFs on smooth reflectance standards with a measurement uncertainty of 1-2 %.

2.3 Snow Specific Surface Area Measurements

Surface snow (just the top few centimeters) samples were collected in nature over the span of three years (winters 2015-2017) and transported in coolers to the nearby US Army's Cold Regions Research Engineering Laboratory (CRREL) in Hanover,

30 New Hampshire. Depth hoar samples, however, were instead grown inside the CRREL at -20 °C using a forced temperature gradient. Snow samples are classified based on X-CT results according to Fierz et al. (2009) (Table 2). Snow SSA was derived from X-CT analysis and contact spectroscopy, as described below.

To determine snow SSA, X-CT was conducted on a class of six snow samples according to Lieb-Lappen et al. (2017). X-ray (40-45 kV, 177-200 micro-Amps) transmission through cylindrical snow samples was measured at rotation steps of 0.3-0.4

degrees. To limit scan times to 15 minutes, exposure time was set to 340 ms at a cubic voxel resolution of 14.9 μm. Processing software enables SSA calculations from 3D morphology results (Pinzer and Schneebeli, 2009).

In some cases, snow samples were scanned several hours or days after snow BRFs were measured. To correct for natural isothermal snow SSA metamorphism while samples were being stored, eq. 2 was applied with time t set equal to the total time elapsed between NERD measurements and X-CT scan times. The unitless growth rate parameters $\tau = 721.2$ or 14400 and growth exponents $n = 2.15$ or 0.32, respectively, were inferred from Ebner et al. (2015) depending on the snow sample type. Applying this correction yielded a SSA decrease between 3 and 5 $\text{m}^2 \text{ kg}^{-1}$.

Snow SSA was also inferred from optical grain size measurements using contact spectroscopy (Painter et al., 2007). Snow reflectance spectra were collected using an ASD FieldSpec4 and a high intensity contact probe with reference to a Spectralon white reference panel. Snow effective radius r_e is determined from the normalized area of the absorption feature centered at approximately 1 μm using a look up table (Nolin and Dozier, 2000). These measurements were conducted inside the CRREL in a cold lab only for the depth hoar (DH_2016) and rounded grains (RG_2015) samples.

2.4 Light Absorbing Particles in Snow Experiments

Snow BRFs and SSA were measured throughout the day in the following dust and BC in snow experiments. Sand particles and hydrophobic BC were sifted multiple times with a salt shaker (with holes of roughly 1 mm diameter) to filter out larger particles. The filtered LAPs were then deposited onto experimental snow plots in an open field in Hanover, New Hampshire on February 10 and February 16, 2017 shortly after fresh snowfall events. For each experiment, one square meter plots of snow were designated as natural (control) or contaminated (experimental). Snow BRFs and SSA were obtained using the NERD and from X-CT analysis, respectively. For each set of NERD measurements, 30 degree and 60 degree BRFs are both recorded four times. BRFs were measured over two different locations within the experimental plot using two photodiodes at each viewing angle (30 and 60 degrees).

2.4.1 Cloudy Sky with Diffuse Ambient Lighting (February 10, 2017)

Early on February 10, experimental plots were loaded with BC until visible darkening was apparent. Snow BRFs were measured shortly after 00:00, 03:00, 06:00 Eastern Standard Time (EST) (during the night), and then periodically throughout the day. Because these plots were well shaded by tall trees, these measurements were used to monitor snow metamorphism without the influence of direct solar illumination. Furthermore, mostly cloudy conditions on February 10 obscured direct solar radiation so that ambient lighting was diffuse.

2.4.2 Clear Sky with Direct Solar Irradiance (February 17, 2017)

On February 17, just a pinch (< 1 g) of BC and 30 g of sand were deposited (quasi-) uniformly over separate one square meter plots. These experimental deposition fluxes were selected to mimic the most extreme LAP loading events observed by Skiles and Painter (2017) in the San Juan Mountains in Colorado. As in the previous experiment, snow BRFs were measured

periodically throughout the day, however, all snow plots were in full view of the clear sky to maximize incident direct solar irradiance.

3 Results and Discussion

3.1 Near-Infrared Reflectance Calculations for Regular Homogenous Ice Particles

To validate the Monte Carlo model for snow applications, we simulated 1.30 and 1.55 μm narrow band black-sky albedo for snow effective radius r_e ranging from 36 to 327 μm (SSA = 80 to 10 m^2kg^{-1}) and compared results with the SNICAR model (Fig. 3). As expected, results from Monte Carlo simulations yield slightly higher hemispheric reflectances for droxtals (for all SSA) and solid hexagonal columns (for SSA > 40 m^2kg^{-1}) than for spheres and from the SNICAR model (Dang et al., 2016). For all particle sizes, Monte Carlo simulations using spherical ice particles generated nearly identical narrow-band albedo values compared to those from Flanner et al. (2007). These results are also similar to the numerical modeling results from Picard et al. (2009) and the analytical solutions from Kokhanovsky and Zege (2004), though for different particle shapes.

To inform on our choice of a snow BRF to SSA calibration function, we calculated BRFs from eq. 4 for various particle SSA ranging from 10 to 80 m^2kg^{-1} (Fig. 4, line graphs). Generally, we found exponential (linear) relationships between 1.30 (1.55) μm BRFs and particle SSAs. Modeled 1.30 μm BRFs are slightly higher at 30 degrees than at 60 degrees for particle SSA > 30 m^2kg^{-1}. For a given particle size, a different shape habit can yield a change in BRFs of as much as 0.1. Monte Carlo modeling results yield the highest reflectances for droxtals and the lowest reflectances for spheres.

3.2 Relating Snow Specific Surface Area to Near-Infrared Bidirectional Reflectance Factors

To calibrate the NERD for snow SSA retrieval, we compared X-CT derived snow SSA with NERD snow BRF measurements (Fig. 4). In general, measured snow BRFs are directly related to snow SSA. At 1.30 μm BRFs range from just under 0.2 (for low SSA) to as high as 0.7 (for high SSA) and are slightly higher at 60 degrees than at 30 degrees. We observed 1.55 μm snow BRFs close to 0 (for low SSA) and as high as 0.2 (for high SSA). We recorded the highest 1.55 μm snow BRFs at 60 degrees for fresh snow (needles). At 1.30 μm, measured 30 degree snow BRFs for varying snow SSA fall within the envelope of Monte Carlo modeled BRFs for all three shape habits (Fig. 4, top left). Modeling results are in closest agreement with measurements at 30 degrees viewing for 1.30 μm. At 1.55 μm, measured BRFs are larger than predicted from modeling across all SSA.

These results demonstrate a considerable spread of BRFs in measurements, across snow samples, and in modeling, across shape habit, for both 1.30 and 1.55 μm and for both 30 and 60 degree viewing angles. The spread in measurements, in particular, indicates a considerable uncertainty in the ability to retrieve snow SSA from measured BRFs. While the 1.30 μm, 30 degree viewing zenith angle BRF combination most closely agrees with modeled BRFs, the 60 degree viewing zenith angle can provide a second estimate of snow SSA. Reporting two snow SSA values using both view angles can provide an estimate of the variability in SSA retrieval resulting from the anisotropy of the snow bidirectional reflectance distribution function in the near-infrared (Dumont et al., 2010).

Our finding of the exponential relationships between snow SSA and 1.30 μm BRFs is consistent with previous studies (Picard et al., 2009; Gallet et al., 2009). Gallet et al. (2009) also identify a linear relationship between 1.55 μm reflectance and snow SSA and use the longer wavelength in their DUFISSS to obtain measurements of high snow SSA (> 60 $\mathrm{m^2kg^{-1}}$). In this study, however, nearly all snow samples are lower than this threshold.

Measured snow BRFs at 1.55 μm are higher than both hemispherical reflectance measurements by Gallet et al. (2009) and Monte Carlo calculations. This discrepancy might be explained by the NERD LEDs, which have full width at half-maximums (FWHM) of 0.130 μm and emit non-negligible light at shorter wavelengths. Supplementary SNICAR and albedo calculations using a broadened FWHM of 0.260 μm support this hypothesis, where values closer to the measured 1.55 μm BRFs are reproduced (Fig. 3, right).

In light of these empirical and numerical results, we propose the following general exponential form relating 1.30 μm snow BRFs to SSA, such that

$$SSA = \alpha \exp(R_{1.30}) + \beta \tag{6}$$

for 1.30 μm snow BRF $R_{1.30}$. Using least squares regression analysis, we estimate "best fit" values for α and β for both 30 and 60 degree viewing zenith angles (see Fig. 5).

Ideally, an empirically derived calibration function would include SSA measurements from multiple methods to mitigate uncertainties associated with collection methods needed for X-CT analysis. Such collection methods can easily change the snow microphysical characteristics and lead to biases in the X-CT derived SSA. As a preliminary validation of eq. 6, we compare snow SSA results to SSA derived from snow effective radius r_e measurements conducted using contact spectroscopy in Fig. 5. Encouragingly, two out of three measurements fall within the bounds of the standard error of the regression. Contact spectroscopy snow SSA values are consistently higher than those calculated from X-CT analysis and are also higher than those determined by eq. 6. This comparison provides a preliminary assessment of the NERD snow BRF to SSA calibration function.

Hereafter, we apply eq. 6 in the following LAP in snow experiments to estimate hourly snow SSA from measured snow BRFs. Because the remainder of this study is concerned with relatively large changes in SSA, approximate SSA retrieval using the NERD is useful to quantitatively assess how added LAPs affect snow grain-size feedback and snow metamorphism.

3.3 Light Absorbing Particles' Effect on Snow Metamorphism

First, to monitor snow metamorphism without solar heating, during the early morning (night) hours on February 10, we deposited BC onto an experimental plot after the previous day's snow fall. Surface temperatures ranged from -14 to -9 °C. We observed low to moderate wind speeds from the early morning hours through the afternoon with partly to mostly cloudy conditions during the day. The 1.30 μm snow BRF measurements conducted shortly after BC application indicate a direct darkening of 0.03 at 30 degrees viewing and 0.05 at 60 degrees viewing. While these decreased BRF values are considerable, this experiment contained heavily contaminated snow with a high BC concentration unlikely to occur in nature. Despite the high BC concentration, BRFs measured at 1.30 (1.55) μm remained within 0.5 and 0.6 (0.1 and 0.2) throughout the day in both contaminated and natural snow (see Fig. 6). X-CT analysis showed small differences in morning (49 $\mathrm{m^2kg^{-1}}$) and afternoon

(48 m^{2}kg^{-1}) snow SSA. Our results indicate that heavy BC loading had little to no effect on snow metamorphism during the 16 hour experiment without direct solar irradiance.

Second, to monitor snow metamorphism occurring after forced large BC and dust deposition events under direct solar illumination, on February 17, we set up a similar experiment in full view of the sun. Surface temperatures ranged from -4 to +2 °C. We observed minimal wind speeds and cloud cover resulting in calm, clear sky conditions. BRF measurements conducted shortly after LAP application indicate minimal direct darkening at 1.30 μm and possibly a small brightening effect by dust at 1.55 μm. In natural snow, 1.30 μm BRFs remained close to 0.5 throughout the day, with the lowest values (0.49) recorded in the afternoon (13:00 EST) and the highest values (0.55) recorded in the morning (08:00 EST) and evening (17:00 EST). 1.55 μm BRFs remained just above 0.1. In the dust loaded plot, snow 1.30 (1.55) μm BRFs decreased rapidly from above 0.5 (0.1) before 10:00 to to below 0.3 (0.05) by 13:00 EST. We found less extreme metamorphism in the lightly contaminated snow with added BC, as BRF measurements decreased from above 0.5 (0.1) to below 0.45 (0.1). 1.30 μm snow BRFs slightly increased thereafter (from 13:00 to 17:00 EST) in both natural and contaminated snow (see Fig. 7). Snow SSA also decreased throughout the day. From X-CT analysis, we found morning snow SSA to be about 50 m^{2}kg^{-1}, which thereafter decreased to 41, 23, and 18 m^{2}kg^{-1} in natural, BC loaded, and dust loaded snow, respectively. NERD derived snow SSA appears to be biased low in the afternoon dust loaded plot. This bias might be an indication of the presence of liquid water that was also visible to the naked eye. X-CT scans performed on this snow sample are representative of refrozen snow and do not conform to the isothermal snow SSA correction (eq. 2) applied to snow samples scanned several hours after collection. In BC loaded plots, we observed a large spatial heterogeneity in measurements, indicating that small BC deposition has a powerful localized effect on snow metamorphism.

These results suggest that extreme LAP deposition can accelerate snow metamorphism. The primary cause of this accelerated process is enhanced absorption of solar radiation by LAP. Surprisingly, added BC had little to no effect on snow metamorphism during cloudy conditions. In the clear sky experiments, LAP enhanced solar absorption at the surface which warmed the snowpack. As the snow surface began to melt, near-infrared reflectance decreased rapidly. Rapidly decreasing near-infrared reflectance is indicative of either the accumulation of liquid water from melting snow or decreasing snow surface SSA.

Accelerated snow metamorphism by dust loading is consistent with the findings of Skiles and Painter (2017). The indirect effect of LAP on snow is also demonstrated by Hadley and Kirchstetter (2012), where the albedo reduction due to the presence of BC in snow is amplified in snow of lower SSA. This enhancement of snow albedo reduction is another source of instability in the snowpack that increases the strength of the snow grain-size feedback. Typical BC deposition events are very small, however, so it is difficult to reproduce natural BC concentrations when adding any BC to a one square meter plot.

4 Conclusions

LAPs in snow accelerated snow metamorphism and enhanced positive grain-size feedback during cloud free, calm weather conditions when surface air temperatures were near 0°C. To observe this effect, we engineered an instrument (i.e., the NERD) that measures 1.30 and 1.55 μm snow BRFs without destroying snow samples. We evaluated the NERD's accuracy, precision,

and responsiveness by testing with idealized Lambertian surfaces before obtaining snow BRFs. Notwithstanding the limitations associated with retrieving precise snow SSA from BRFs, we proposed an analytical calibration function relating snow SSA to 1.30 μm BRFs. Our results lead to the conclusion that the NERD can provide estimates of snow SSA to within +/- 10 $m^2 kg^{-1}$.

The NERD will serve to further study the effects of LAPs on snow metamorphism and to explore the spatial heterogeneity of snow SSA. Because it can also operate quickly, NERD measurements can complement satellite borne observations during narrow sampling windows. To fulfill these pursuits, however, a more comprehensive snow SSA measurement uncertainty assessment is needed to fully validate the NERD technique. Validation would also include additional independent measurement methods on snow samples with a larger snow SSA span from a variety of environmental conditions and further experimentation into the small scale effects on snow BRF measurements. Further investigation of the natural variability of snow near the surface and the related quantitative uncertainties regarding the NERD snow SSA retrieval method will be the subject of a follow on study. Such a study will also include snow of higher SSA to determine the utility of 1.55 μm snow BRFs in measuring fresh snow of extremely high SSA, as demonstrated by Gallet et al. (2009). This would help expand the utility of the NERD measurement technique for future Arctic and Antarctic campaigns, building on the polar studies conducted by Legagneux et al. (2002) and Libois et al. (2015).

Code and data availability. Plot data referenced in this manuscript and associated Python scripts used to generate figures are made available via the University of Michigan's Deep Blue data repository (Schneider and Flanner, 2018).

Appendix A: NERD Photodiode Current Amplifiers

To detect reflected radiance signals, photodiodes are reverse biased to induce currents linearly related to the amount of light incident on its active region. Because these light signals are reflected from the experimental surface, the currents induced by the photodiodes are very small (nano- to micro-Amps). To measure the small currents, the photodiodes are connected to transimpedance amplifiers. The transimpedance amplifier circuits convert and amplify the small photodiode currents into measurable voltage signals.

Two NERDs are engineered with different photodiode current amplifications. Photodiode current amplification is determined by the feedback resistance in the transimpedance amplifier circuits. Active low pass filters are applied between the amplifier and the analog-to-digital converter (ADC) to reduce noise. This filter is designed to have a time constant of less than 0.5 seconds to achieve balance between adequate noise reduction and speed.

Competing interests. Mark Flanner is currently an editor for *The Cryosphere*. We are not aware of any other competing interests associated with the publication of this manuscript.

Acknowledgements. This work is funded, in part, by the National Science Foundation, grant number ARC-1253154.

The authors would like to thank their colleagues at the Cold Regions Research and Engineering Laboratory (CRREL) in Hanover, New Hampshire for generous support. In particular, thanks to Zoe Courville and John Fegyveresi for their hospitality and guidance navigating the facilities at CRREL. We also thank Ross Lieblappen for sharing his micro-computed tomography expertise through providing a thorough tutorial for running and analyzing snow scans.

The authors are thankful for reviews from three referees (including Marie Dumont). These detailed reviews were helpful in reorganizing the manuscript and improving the presentation of the key results.

References

Arnaud, L., Picard, G., Champollion, N., Domine, F., Gallet, J., Lefebvre, E., Fily, M., and Barnola, J.: Measurement of vertical profiles of snow specific surface area with a 1 cm resolution using infrared reflectance: instrument description and validation, Journal of Glaciology, 57, 17–29, https://doi.org/10.3189/002214311795306664, https://www.cambridge.org/core/product/identifier/S0022143000204607/type/journal_article, 2011.

Bond, T. C., Doherty, S. J., Fahey, D. W., Forster, P. M., Berntsen, T., DeAngelo, B. J., Flanner, M. G., Ghan, S., Kärcher, B., Koch, D., Kinne, S., Kondo, Y., Quinn, P. K., Sarofim, M. C., Schultz, M. G., Schulz, M., Venkataraman, C., Zhang, H., Zhang, S., Bellouin, N., Guttikunda, S. K., Hopke, P. K., Jacobson, M. Z., Kaiser, J. W., Klimont, Z., Lohmann, U., Schwarz, J. P., Shindell, D., Storelvmo, T., Warren, S. G., and Zender, C. S.: Bounding the role of black carbon in the climate system: A scientific assessment: BLACK CARBON IN THE CLIMATE SYSTEM, Journal of Geophysical Research: Atmospheres, 118, 5380–5552, https://doi.org/10.1002/jgrd.50171, http://doi.wiley.com/10.1002/jgrd.50171, 2013.

Brandt, R. E. and Warren, S. G.: Solar-heating rates and temperature profiles in Antarctic snow and ice, Journal of Glaciology, 39, 99–110, https://doi.org/10.3189/S0022143000015756, https://www.cambridge.org/core/product/identifier/S0022143000015756/type/journal_article, 1993.

Dang, C., Fu, Q., and Warren, S. G.: Effect of Snow Grain Shape on Snow Albedo, Journal of the Atmospheric Sciences, 73, 3573–3583, https://doi.org/10.1175/JAS-D-15-0276.1, http://journals.ametsoc.org/doi/10.1175/JAS-D-15-0276.1, 2016.

Domine, F., Salvatori, R., Legagneux, L., Salzano, R., Fily, M., and Casacchia, R.: Correlation between the specific surface area and the short wave infrared (SWIR) reflectance of snow, Cold Regions Science and Technology, 46, 60–68, https://doi.org/10.1016/j.coldregions.2006.06.002, http://linkinghub.elsevier.com/retrieve/pii/S0165232X06000735, 2006.

Dumont, M., Brissaud, O., Picard, G., Schmitt, B., Gallet, J.-C., and Arnaud, Y.: High-accuracy measurements of snow Bidirectional Reflectance Distribution Function at visible and NIR wavelengths – comparison with modelling results, Atmospheric Chemistry and Physics, 10, 2507–2520, https://doi.org/10.5194/acp-10-2507-2010, http://www.atmos-chem-phys.net/10/2507/2010/, 2010.

Ebner, P. P., Schneebeli, M., and Steinfeld, A.: Tomography-based monitoring of isothermal snow metamorphism under advective conditions, The Cryosphere, 9, 1363–1371, https://doi.org/10.5194/tc-9-1363-2015, https://www.the-cryosphere.net/9/1363/2015/, 2015.

Fierz, C., Armstrong, R., Durand, Y., Etchevers, P., Greene, E., McClung, D., Nishimura, K., Satyawali, P., and Sokratov, S.: The International Classification for Seasonal Snow on the Ground, 2009.

Flanner, M. G. and Zender, C. S.: Linking snowpack microphysics and albedo evolution, Journal of Geophysical Research, 111, https://doi.org/10.1029/2005JD006834, http://doi.wiley.com/10.1029/2005JD006834, 2006.

Flanner, M. G., Zender, C. S., Randerson, J. T., and Rasch, P. J.: Present-day climate forcing and response from black carbon in snow, Journal of Geophysical Research, 112, https://doi.org/10.1029/2006JD008003, http://doi.wiley.com/10.1029/2006JD008003, 2007.

Flanner, M. G., Zender, C. S., Hess, P. G., Mahowald, N. M., Painter, T. H., Ramanathan, V., and Rasch, P. J.: Springtime warming and reduced snow cover from carbonaceous particles, Atmospheric Chemistry and Physics, 9, 2481–2497, https://doi.org/10.5194/acp-9-2481-2009, http://www.atmos-chem-phys.net/9/2481/2009/, 2009.

Gallet, J.-C., Domine, F., Zender, C. S., and Picard, G.: Measurement of the specific surface area of snow using infrared reflectance in an integrating sphere at 1310 and 1550 nm, The Cryosphere, 3, 167–182, https://doi.org/10.5194/tc-3-167-2009, http://www.the-cryosphere.net/3/167/2009/, 2009.

Gallet, J.-C., Domine, F., and Dumont, M.: Measuring the specific surface area of wet snow using 1310 nm reflectance, The Cryosphere, 8, 1139–1148, https://doi.org/10.5194/tc-8-1139-2014, https://www.the-cryosphere.net/8/1139/2014/, 2014.

Gergely, M., Wolfsperger, F., and Schneebeli, M.: Simulation and Validation of the InfraSnow: An Instrument to Measure Snow Optically Equivalent Grain Size, IEEE Transactions on Geoscience and Remote Sensing, 52, 4236–4247, https://doi.org/10.1109/TGRS.2013.2280502, http://ieeexplore.ieee.org/document/6606890/, 2014.

Grenfell, T. C., Warren, S. G., and Mullen, P. C.: Reflection of solar radiation by the Antarctic snow surface at ultraviolet, visible, and near-infrared wavelengths, Journal of Geophysical Research, 99, 18 669, https://doi.org/10.1029/94JD01484, http://doi.wiley.com/10.1029/94JD01484, 1994.

Hadley, O. L. and Kirchstetter, T. W.: Black-carbon reduction of snow albedo, Nature Climate Change, 2, 437–440, https://doi.org/10.1038/nclimate1433, http://www.nature.com/articles/nclimate1433, 2012.

Hagenmuller, P., Matzl, M., Chambon, G., and Schneebeli, M.: Sensitivity of snow density and specific surface area measured by microtomography to different image processing algorithms, The Cryosphere, 10, 1039–1054, https://doi.org/10.5194/tc-10-1039-2016, https://www.the-cryosphere.net/10/1039/2016/, 2016.

Hall, A.: The Role of Surface Albedo Feedback in Climate, Journal of Climate, 17, 1550–1568, https://doi.org/10.1175/1520-0442(2004)017<1550:TROSAF>2.0.CO;2, http://journals.ametsoc.org/doi/abs/10.1175/1520-0442%282004%29017%3C1550%3ATROSAF%3E2.0.CO%3B2, 2004.

Hudson, S. R., Warren, S. G., Brandt, R. E., Grenfell, T. C., and Six, D.: Spectral bidirectional reflectance of Antarctic snow: Measurements and parameterization, Journal of Geophysical Research, 111, https://doi.org/10.1029/2006JD007290, http://doi.wiley.com/10.1029/2006JD007290, 2006.

Kaempfer, T. U., Hopkins, M. A., and Perovich, D. K.: A three-dimensional microstructure-based photon-tracking model of radiative transfer in snow, Journal of Geophysical Research, 112, https://doi.org/10.1029/2006JD008239, http://doi.wiley.com/10.1029/2006JD008239, 2007.

Kokhanovsky, A. A. and Zege, E. P.: Scattering optics of snow, Applied Optics, 43, 1589, https://doi.org/10.1364/AO.43.001589, https://www.osapublishing.org/abstract.cfm?URI=ao-43-7-1589, 2004.

Legagneux, L. and Domine, F.: A mean field model of the decrease of the specific surface area of dry snow during isothermal metamorphism: MODEL OF SNOW SURFACE AREA DECREASE, Journal of Geophysical Research: Earth Surface, 110, n/a–n/a, https://doi.org/10.1029/2004JF000181, http://doi.wiley.com/10.1029/2004JF000181, 2005.

Legagneux, L., Cabanes, A., and Dominé, F.: Measurement of the specific surface area of 176 snow samples using methane adsorption at 77 K: MEASUREMENT USING METHANE ADSORPTION AT 77 K, Journal of Geophysical Research: Atmospheres, 107, ACH 5–1–ACH 5–15, https://doi.org/10.1029/2001JD001016, http://doi.wiley.com/10.1029/2001JD001016, 2002.

Legagneux, L., Taillandier, A.-S., and Domine, F.: Grain growth theories and the isothermal evolution of the specific surface area of snow, Journal of Applied Physics, 95, 6175–6184, https://doi.org/10.1063/1.1710718, http://aip.scitation.org/doi/10.1063/1.1710718, 2004.

Libois, Q., Picard, G., Arnaud, L., Dumont, M., Lafaysse, M., Morin, S., and Lefebvre, E.: Summertime evolution of snow specific surface area close to the surface on the Antarctic Plateau, The Cryosphere, 9, 2383–2398, https://doi.org/10.5194/tc-9-2383-2015, https://www.the-cryosphere.net/9/2383/2015/, 2015.

Lieb-Lappen, R., Golden, E., and Obbard, R.: Metrics for interpreting the microstructure of sea ice using X-ray micro-computed tomography, Cold Regions Science and Technology, 138, 24 – 35, https://doi.org/https://doi.org/10.1016/j.coldregions.2017.03.001, http://www.sciencedirect.com/science/article/pii/S0165232X17301040, 2017.

Malinka, A. V.: Light scattering in porous materials: Geometrical optics and stereological approach, Journal of Quantitative Spectroscopy and Radiative Transfer, 141, 14–23, https://doi.org/10.1016/j.jqsrt.2014.02.022, https://linkinghub.elsevier.com/retrieve/pii/S002240731400079X, 2014.

Matzl, M. and Schneebeli, M.: Measuring specific surface area of snow by near-infrared photography, Journal of Glaciology, 52, 558–564, https://doi.org/10.3189/172756506781828412, https://www.cambridge.org/core/product/identifier/S0022143000209301/type/journal_article, 2006.

Nicodemus, F., Richmond, J., Hsia, J., Ginsberg, I., and Limperis, T.: Geometrical considerations and nomenclature for reflectance, National Bureau of Standards, 1977.

Nolin, A. W. and Dozier, J.: A Hyperspectral Method for Remotely Sensing the Grain Size of Snow, Remote Sensing of Environment, 74, 207 – 216, https://doi.org/https://doi.org/10.1016/S0034-4257(00)00111-5, http://www.sciencedirect.com/science/article/pii/S0034425700001115, 2000.

Painter, T. H., Molotch, N. P., Cassidy, M., Flanner, M., and Steffen, K.: Contact spectroscopy for determination of stratigraphy of snow optical grain size, Journal of Glaciology, 53, 121–127, https://doi.org/10.3189/172756507781833947, https://www.cambridge.org/core/product/identifier/S0022143000201846/type/journal_article, 2007.

Picard, G., Arnaud, L., Domine, F., and Fily, M.: Determining snow specific surface area from near-infrared reflectance measurements: Numerical study of the influence of grain shape, Cold Regions Science and Technology, 56, 10–17, https://doi.org/10.1016/j.coldregions.2008.10.001, http://linkinghub.elsevier.com/retrieve/pii/S0165232X08001602, 2009.

Pinzer, B. R. and Schneebeli, M.: Snow metamorphism under alternating temperature gradients: Morphology and recrystallization in surface snow, Geophysical Research Letters, 36, https://doi.org/10.1029/2009GL039618, http://doi.wiley.com/10.1029/2009GL039618, 2009.

Qian, Y., Yasunari, T. J., Doherty, S. J., Flanner, M. G., Lau, W. K. M., Ming, J., Wang, H., Wang, M., Warren, S. G., and Zhang, R.: Light-absorbing particles in snow and ice: Measurement and modeling of climatic and hydrological impact, Advances in Atmospheric Sciences, 32, 64–91, https://doi.org/10.1007/s00376-014-0010-0, http://link.springer.com/10.1007/s00376-014-0010-0, 2015.

Qu, X. and Hall, A.: What Controls the Strength of Snow-Albedo Feedback?, Journal of Climate, 20, 3971–3981, https://doi.org/10.1175/JCLI4186.1, http://journals.ametsoc.org/doi/abs/10.1175/JCLI4186.1, 2007.

Ramella-Roman, J. C., Prahl, S. A., and Jacques, S. L.: Three Monte Carlo programs of polarized light transport into scattering media: part I, Optics Express, 13, 4420, https://doi.org/10.1364/OPEX.13.004420, https://www.osapublishing.org/oe/abstract.cfm?uri=oe-13-12-4420, 2005.

Schneider, A. and Flanner, M.: Supporting data for the Near-Infrared Emitting and Reflectance-Monitoring Dome, https://doi.org/10.7302/Z23F4MVC, http://deepblue.lib.umich.edu/data/concern/generic_works/79407x76d, type: dataset, 2018.

Skiles, S. M. and Painter, T.: Daily evolution in dust and black carbon content, snow grain size, and snow albedo during snowmelt, Rocky Mountains, Colorado, Journal of Glaciology, 63, 118–132, https://doi.org/10.1017/jog.2016.125, https://www.cambridge.org/core/product/identifier/S0022143016001258/type/journal_article, 2017.

Skiles, S. M., Flanner, M., Cook, J. M., Dumont, M., and Painter, T. H.: Radiative forcing by light-absorbing particles in snow, Nature Climate Change, 8, 964–971, https://doi.org/10.1038/s41558-018-0296-5, http://www.nature.com/articles/s41558-018-0296-5, 2018.

Smith, B. E., Gardner, A., Schneider, A., and Flanner, M.: Modeling biases in laser-altimetry measurements caused by scattering of green light in snow, Remote Sensing of Environment, 215, 398–410, https://doi.org/10.1016/j.rse.2018.06.012, https://linkinghub.elsevier.com/retrieve/pii/S0034425718302918, 2018.

van de Hulst, H.: Asymptotic fitting, a method for solving anisotropic transfer problems in thick layers, Journal of Computational Physics, 3, 291–306, https://doi.org/10.1016/0021-9991(68)90023-5, https://linkinghub.elsevier.com/retrieve/pii/0021999168900235, 1968.

Vouk, V.: Projected Area of Convex Bodies, Nature, 162, 330–331, https://doi.org/10.1038/162330a0, http://www.nature.com/articles/162330a0, 1948.

5   Wang, X. and Baker, I.: Evolution of the specific surface area of snow during high-temperature gradient metamorphism, Journal of Geophysical Research: Atmospheres, 119, 13,690–13,703, https://doi.org/10.1002/2014JD022131, http://doi.wiley.com/10.1002/2014JD022131, 2014.

Warren, S. G. and Wiscombe, W. J.: A Model for the Spectral Albedo of Snow. II: Snow Containing Atmospheric Aerosols, Journal of the Atmospheric Sciences, 37, 2734–2745, https://doi.org/10.1175/1520-0469(1980)037<2734:AMFTSA>2.0.CO;2, http://journals.ametsoc.

10   org/doi/abs/10.1175/1520-0469%281980%29037%3C2734%3AAMFTSA%3E2.0.CO%3B2, 1980.

Yang, P., Bi, L., Baum, B. A., Liou, K.-N., Kattawar, G. W., Mishchenko, M. I., and Cole, B.: Spectrally Consistent Scattering, Absorption, and Polarization Properties of Atmospheric Ice Crystals at Wavelengths from 0.2 to 100 μm, Journal of the Atmospheric Sciences, 70, 330–347, https://doi.org/10.1175/JAS-D-12-039.1, http://journals.ametsoc.org/doi/abs/10.1175/JAS-D-12-039.1, 2013.
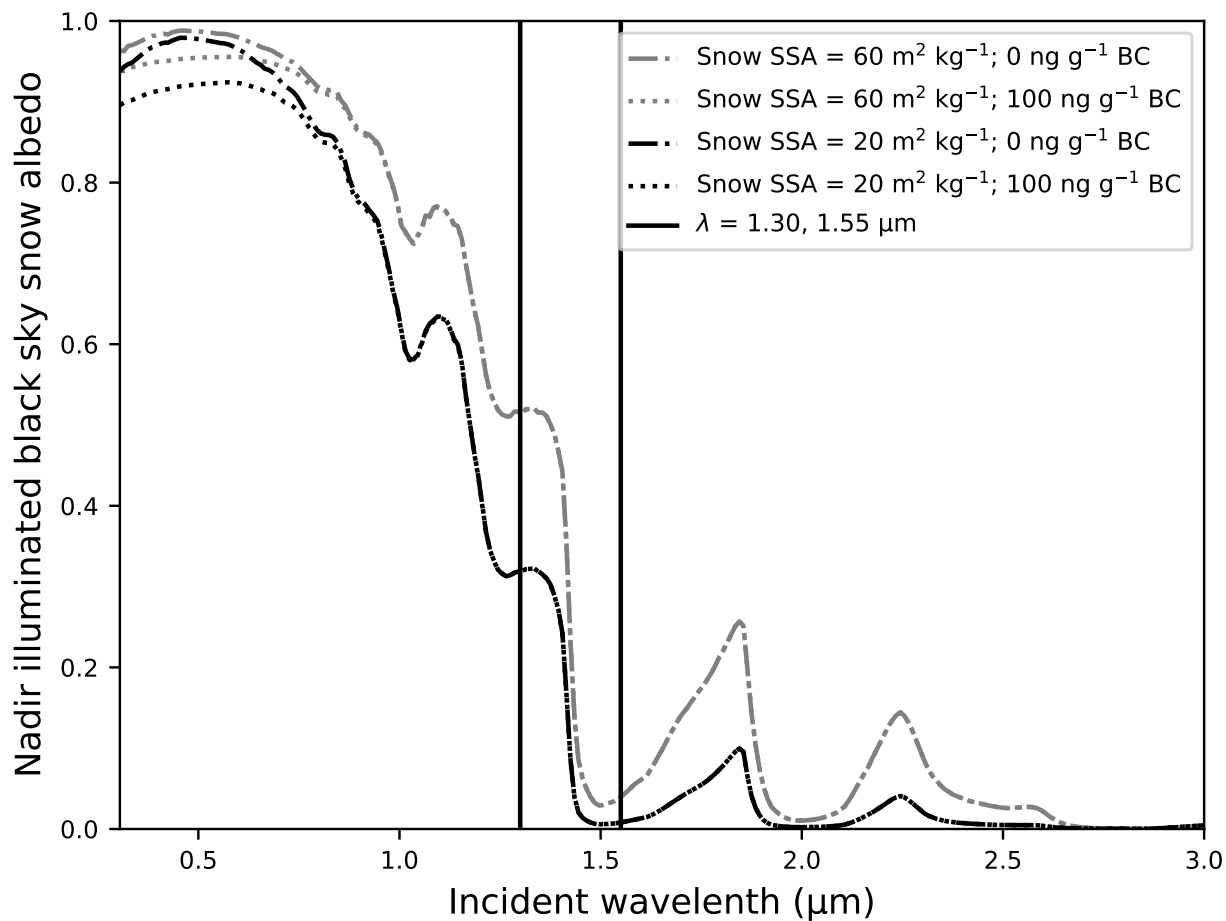
Figure 1. Black sky spectral snow albedo under nadir illumination. Snow albedo is simulated by the Snow, Ice, and Aerosol Radiation (SNICAR) model (Flanner et al., 2007). Dashed-dotted curves represent clean snow of medium-high SSA (60 m^2 kg^{-1}, gray) and medium-low SSA (20 m^2 kg^{-1}, black) to show the dependence of snow albedo on snow SSA. Dotted curves represent contaminated snow with uncoated black carbon (BC) particulate concentrations of 100 ng g^{-1}.
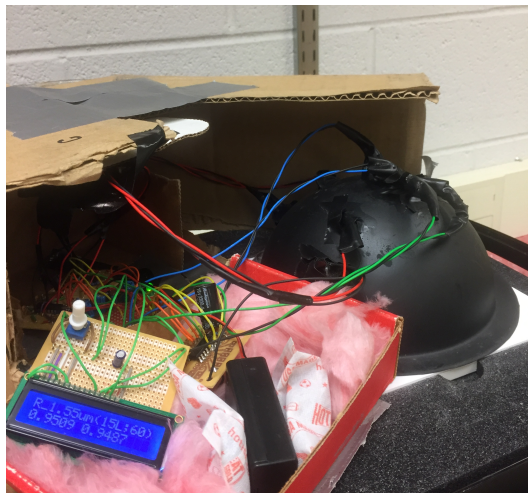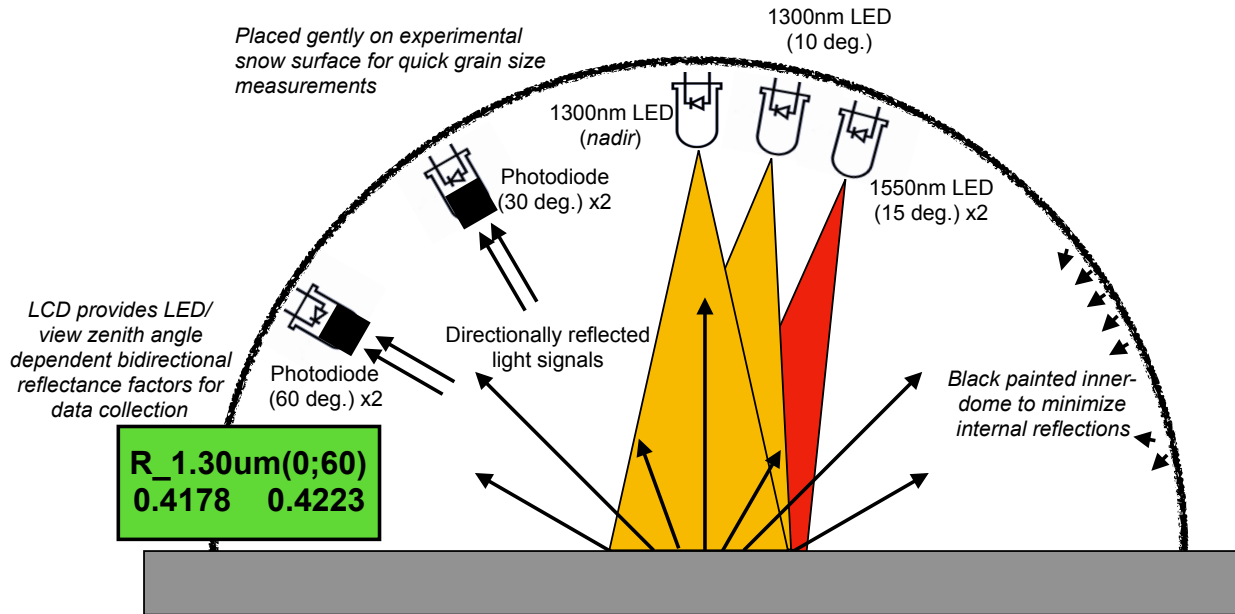
Figure 2. Near-Infrared Emitting and Reflectance-Monitoring Dome (NERD) schematic (top) and photographs (bottom). The photograph on the bottom right shows the (radial) placement of photodiodes and LEDs (toward the center) within the dome.
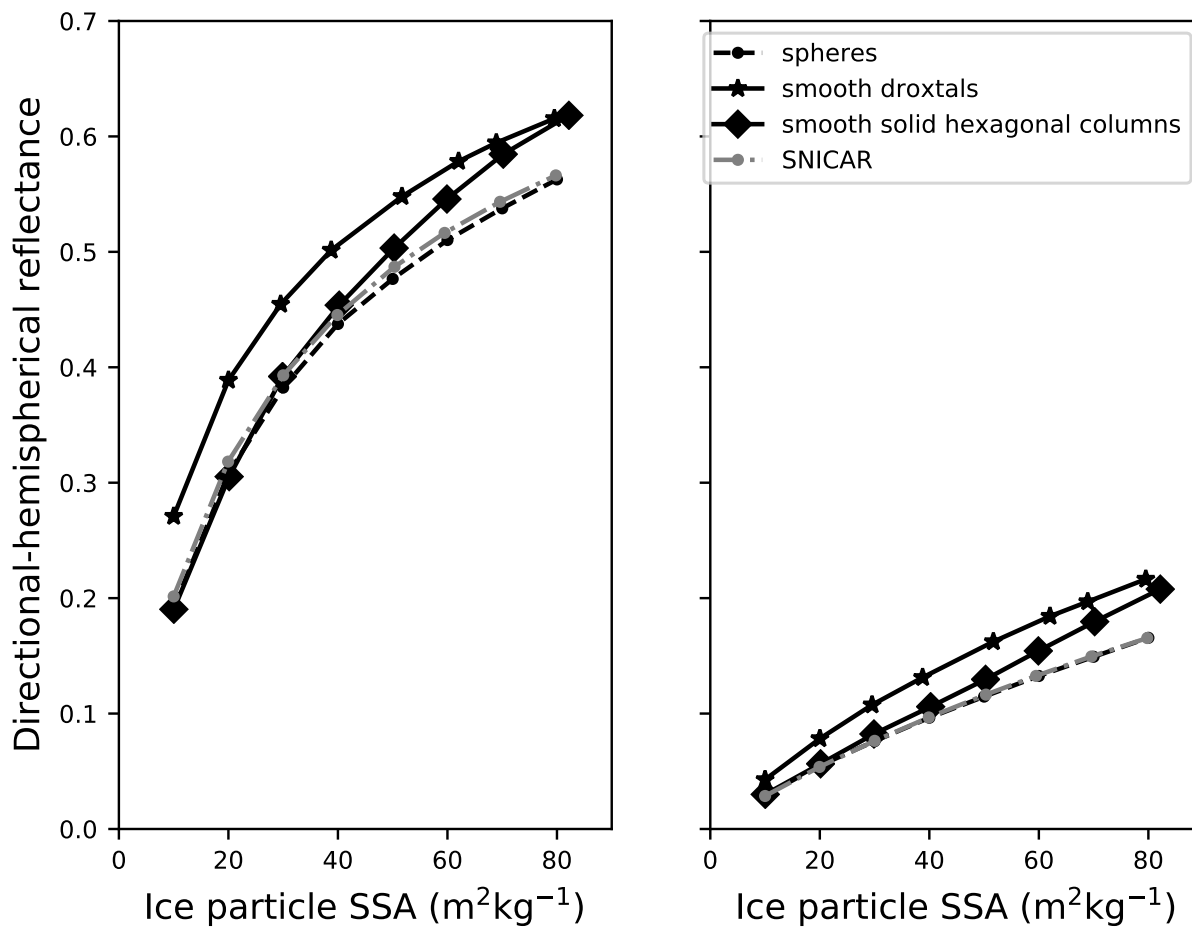
Figure 3. Modeled 1.30 μm nadir (left) and 1.55 μm 15 degree (right) directional hemispherical reflectance for various snow SSA. Solid line segments connect albedo calculations from Monte Carlo simulations of light scattering in snow mediums comprised of droxtals (stars) and solid hexagonal columns (diamonds). Circles connected by dashed / dotted line segments connect snow albedo calculations modeled as spherical ice particles; from Monte Carlo modeling (black) and from the Snow, Ice, and Aerosol Radiation (SNICAR) online model (gray).
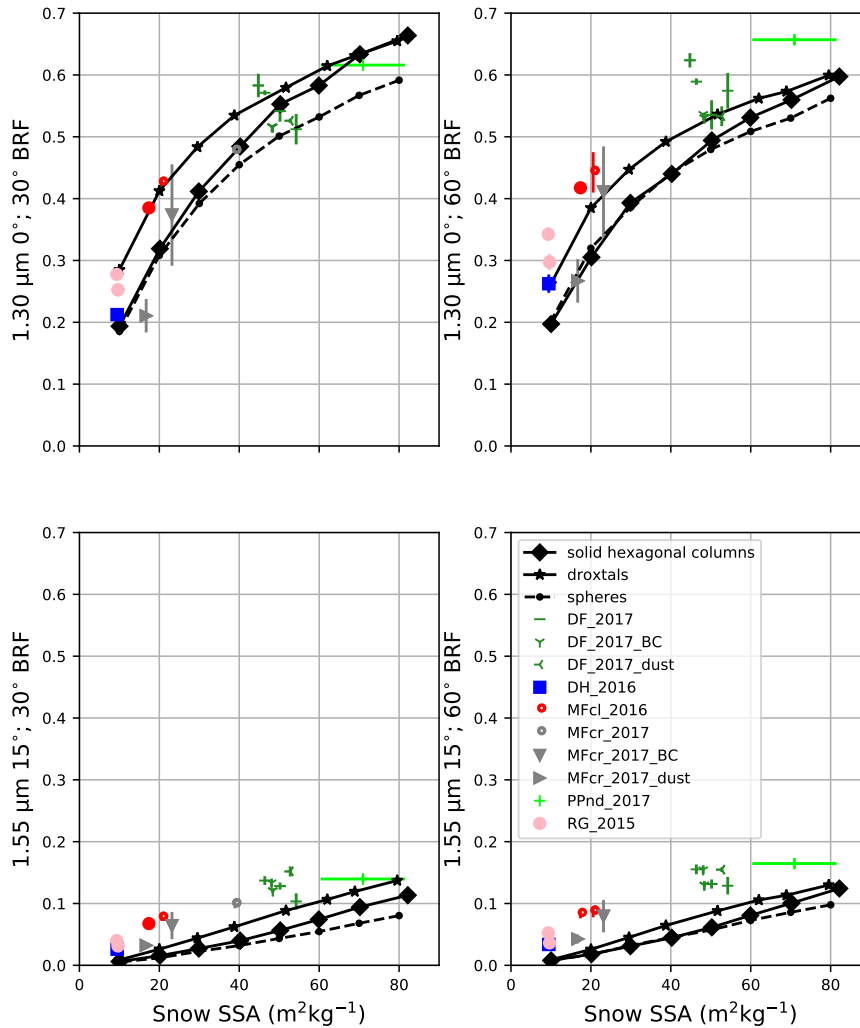
Figure 4. NERD SSA Calibration. All panels contain NERD measured and Monte Carlo modeled (black) BRFs (1.30 μm, top; 1.55 μm, bottom; 30 degrees viewing, left; 60 degrees viewing, right) scattered against snow SSA. NERD BRFs are scattered against X-CT derived snow SSA. Line segments connect Monte Carlo modeled BRFs of snow mediums comprised of spheres (filled circles, dashed lines), droxtals (stars, solid lines), and solid hexagonal columns (diamonds, solid lines). Snow sample key codes, symbols, and colors conform with the physical snow classification standards defined by Fierz et al. (2009) (Table 2). Vertical error bars on NERD BRFs represent standard deviations calculated from multiple azimuthal samples. Horizontal error bars on X-CT derived SSA, where present, represent standard deviations from multiple scans on similar snow samples.
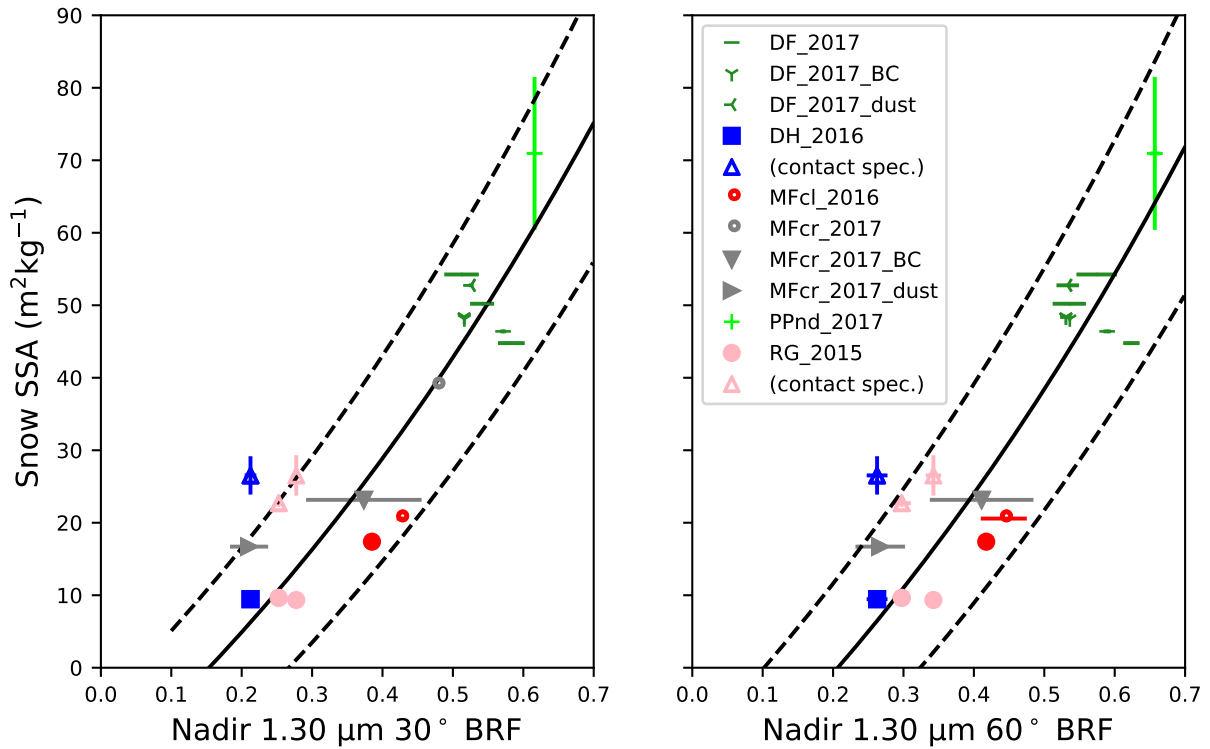
Figure 5. Snow 1.3 μm BRF to SSA exponential regressions. Markers with standard error bars represent SSA, measured with X-CT[*], scattered against nadir 1.30 μm 30 (left) and 60 (right) degree BRFs, measured by the NERD. Solid curves represent exponential regression functions and dashed curves represent standard errors of the regressions, such that at 30 degrees viewing, α = 88.7 (+/- 9.50) m^{2}kg^{-1} and β = -103 m^{2}kg^{-1}; and at 60 degrees viewing, α = 91.7 (+/- 10.13) m^{2}kg^{-1} and β = -113 m^{2}kg^{-1}.

[*]Hollow triangles (blue, depth hoar; pink, rounded grains) represent snow SSA measurements derived from contact spectroscopy.
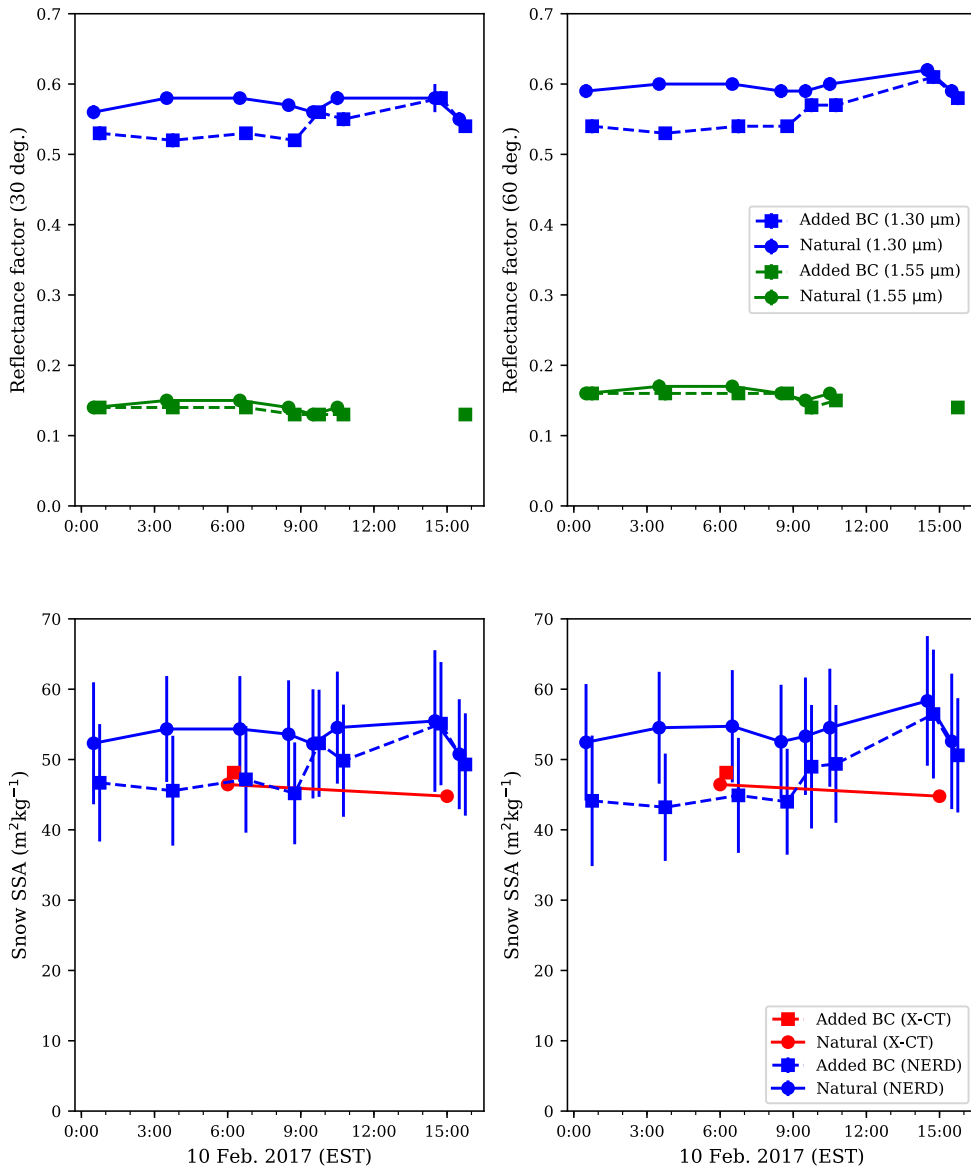
Figure 6. February 10 Control Results (mostly cloudy). All panels contain NERD measurement data collected from 00:00 through 17:00 Eastern Standard Time (EST) on February 10, 2017. Filled circles connected by solid lines represent measurements on natural snow. Filled squares connected by dashed lines represent measurements on snow heavily contaminated by hydrophobic BC. In the top row, blue (green) curves represent 1.30 μm (1.55 μm) BRFs at 30 degrees viewing – on the left – and 60 degrees viewing – on the right. Error bars represent standard errors calculated from sample averages from as many as eight locations within each square meter plot. In the bottom figure, blue curves represent NERD calibrated SSA from 30, left, and 60, right, degree viewing BRFs. Red curves represent SSA derived from X-CT scans. Error bars represent NERD calibration uncertainty computed from regression analysis (standard errors of the gradients).
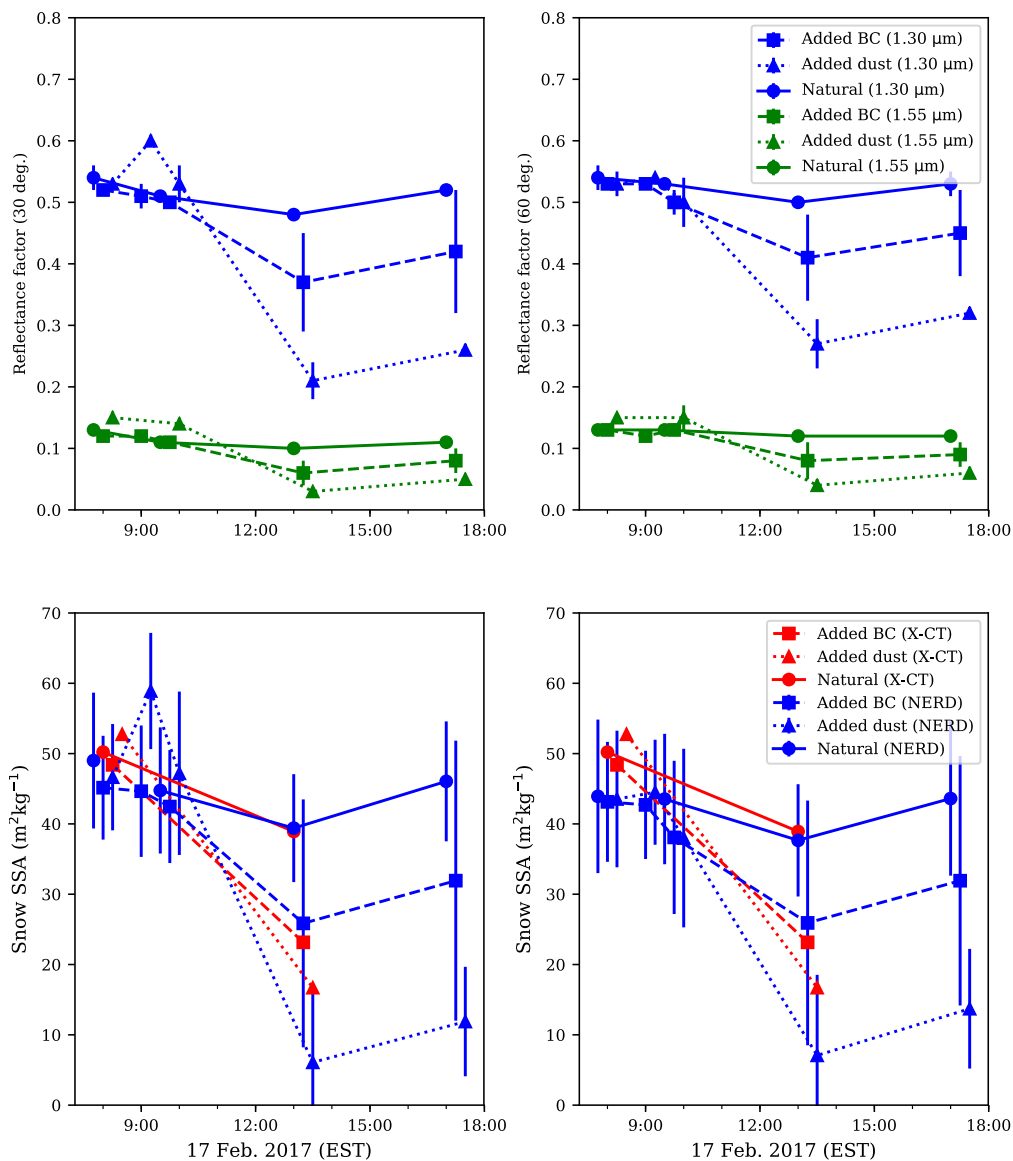
Figure 7. February 17 Experimental Results (clear sky). All panels contain NERD measurement data collected from 07:00 through 17:00 EST on February 17, 2017. Filled circles connected by solid lines represent measurements on natural snow. Filled squares connected by dashed lines represent measurements on snow lightly contaminated (< 1 gm^{-2}) by hydrophobic BC. Triangles connected by dotted lines represent measurements on snow contaminated by dust (30 gm^{-2}). In the top row, blue (green) curves represent 1.30μm (1.55μm) BRFs at 30 degrees viewing – on the left – and 60 degrees viewing – on the right. Error bars represent standard errors calculated from sample averages from as many as eight locations within each square meter plot. In the bottom figure, blue curves represent NERD calibrated SSA from 30, left, and 60, right, degree viewing BRFs. Red curves represent SSA derived from X-CT scans. Error bars represent NERD calibration uncertainty computed from regression analysis (standard errors of the gradients).

Table 1. NERD Lambertian Reflectance Measurements. Tabulated values represent median BRFs ($R(\theta_i; \theta_r)$) calculated for n samples of measurements from Lambertian Reflectance targets with nominal reflectances of ρ_L (RMS difference in parenthesis). Linear regressions for each wavelength (λ) are calculated from $n_1 + n_2 = N$ samples.

$\lambda = 1.30$ μm

n	ρ_L	$R(0°; 30°)$	$R(0°; 60°)$	$R(10°; 30°)$	$R(10°; 60°)$
10	0.422	0.399 (0.021)	0.422 (0.016)	0.415 (0.015)	0.434 (0.015)
10	0.951	0.939 (0.013)	0.944 (0.015)	0.958 (0.018)	0.952 (0.010)
N		Linear regression; $\hat{R}(\rho_L) = A\rho_L + B$			
20	$\hat{R} =$	$\{1.023\rho_L - 0.028,$	$0.987\rho_L + 0.007,$	$1.031\rho_L - 0.024,$	$0.980\rho_L - 0.018\}$

$\lambda = 1.55$ μm

n	ρ_L	$R(15_a^\circ; 30°)$	$R(15_a^\circ; 60°)$	$R(15_b^\circ; 30°)$	$R(15_b^\circ; 60°)$
10	0.413	0.410 (0.009)	0.420 (0.017)	0.411 (0.008)	0.420 (0.021)
6	0.944	0.959 (0.012)	0.963 (0.019)	0.960 (0.013)	0.964 (0.020)
N		Linear regression; $\hat{R}(\rho_L) = A\rho_L + B$			
16	$\hat{R} =$	$\{1.028\rho_L - 0.016,$	$1.016\rho_L + 0.003,$	$1.026\rho_L - 0.014,$	$1.011\rho_L + 0.009\}$

Table 2. Snow Sample Physical Classification (Fierz et al., 2009). Snow density, porosity, and specific surface area (SSA) are calculated from X-ray micro-computed tomography.

Grain shape	Density (kg m^{-3})	Porosity (%)	SSA (m^{2}kg^{-1})	LAPs	Figure key code
Needles	110	88	66	None	PPnd_2017
Decomposing precip. particles	170	82	54	None or w/ dust or BC	DC_2017
Melt-freeze crust	310	66	23	None or w/ dust or BC	MFcr_2017
Clustered rounded grains	350	62	19	None	MFcl_2016
Depth hoar	320	65	9	None	DH_2016
Rounded grains	610	33	9	None	RG_2015